Detecting highly entangled states with a joint qubit readout

J. M. Chow,[1] L. DiCarlo,[1] J. M. Gambetta,[2] A. Nunnenkamp,[1] Lev S. Bishop,[1] L. Frunzio,[1] M. H. Devoret,[1] S. M. Girvin,[1] and R. J. Schoelkopf[1]

[1]*Departments of Physics and Applied Physics, Yale University, New Haven, Connecticut 06520, USA*

[2]*Institute for Quantum Computing and Department of Physics and Astronomy, University of Waterloo, Waterloo, Ontario N2L 3G1, Canada*

(Received 18 February 2010; published 17 June 2010)

A single-channel joint readout is used to analyze highly entangled two-qubit states in a circuit quantum electrodynamics architecture. The measurement model for the readout is fully characterized, demonstrating a large sensitivity to two-qubit correlations. We quantify the high degree of entanglement by measuring a violation of the Clauser-Horne-Shimony-Holt inequality with a value of 2.61 ± 0.04, without optimizing the preparation of the two-qubit state. In its present form, this joint readout can resolve improvements to the fidelity of two-qubit operations and be extended to three or four qubits.

DOI: 10.1103/PhysRevA.81.062325 PACS number(s): 03.67.Ac, 42.50.Pq, 85.25.−j

I. INTRODUCTION

Measuring entanglement, nonclassical correlations, between qubits is critical for experimental progress in quantum information science. In any experiment one obtains information about the quantum system only through observing the output of a detector, whose imperfections can introduce bias and noise. Therefore, to make precise statements about the entanglement, or other intrinsic properties of quantum states, it is necessary to have a full understanding of the measurement process.

In more developed quantum information processing architectures, such as those employing photons or trapped ions, the relationship between a quantum state and the quantities observed has been well established. In addition, the fidelity of single-shot measurements can be very high (∼99.99% for ions [1]). Consequently, the difficulties of calibration are minimized and the paradigm for correlation measurements [2,3] is to record coincidences between individual detector "clicks" and build statistics through repetition. However, in the context of solid-state systems, the details of the measurement process itself are not fully understood and are an area of active research and recent progress. Single-shot individual qubit measurements have been technically challenging, and the readout fidelity is not yet as high as the fidelity of qubit operations (∼98%–99% for single-qubit gates [4,5]). Each individual readout channel can provide an additional path for decoherence and must also be calibrated. An example of the need for calibration is measurement cross-talk, which can be significant in circuit-based architectures [6] but has now been suppressed to the 0.5% level using an on-chip cavity as a filter [7]. Recently, the single-shot fidelity of independent readouts of superconducting qubits has also been improved [7,8] to ∼95% and violation of a Bell inequality has been achieved [7].

In this work, we pursue an alternative approach by employing a *single* joint, or quadratic, readout [9–12] realized as the microwave resonator of a circuit quantum electrodynamics architecture [13], where the measurement operator itself includes multiqubit correlations. We first characterize the form of the measurement operator for this joint readout. Taking advantage of good state initialization [14] and high-fidelity single-qubit gates [5], we can place bounds of 2% on systematic deviations from the ideal joint measurement. This is similar to determining the systematic errors, such as cross-talk [15], in individual readouts. The high relative sensitivity to two-qubit correlations in the measurement operator, or *jointness*, makes the joint readout as efficient for measuring qubit correlations as for single-qubit polarizations. Since the correlation is performed before averaging, the classical amplifier noise that limits the single-shot readout fidelity enters only as a statistical error, and it can be largely eliminated with sufficient repetition. Using this readout, we then demonstrate a high degree of entanglement by measuring a large violation of a Clauser-Horne-Shimony-Holt (CHSH) inequality [16], with a value of 2.61 ± 0.04, without optimizing for the target state.

II. JOINT READOUT

A. Model

Our device consists of two transmon qubits [17,18] located at opposite ends of a superconducting transmission-line resonator (The experimental setup and transmon parameters are given in Appendices A and B). Arbitrary single-qubit x- and y-rotations [5] are performed by employing a derivative pulse-shaping technique [19,20], resulting in single-qubit error rates of $<1\%$. Local flux-bias lines tune the qubit transition frequencies, allowing nanosecond control of a two-qubit $Z^{\mathrm{L}}Z^{\mathrm{R}}$ interaction that implements [21] conditional-phase (c-Phase) gates [with $Z^{\mathrm{L(R)}} = \sigma_z^{\mathrm{L(R)}}$ being the single-qubit Pauli z operator on the left (right) qubit]. Combining single-qubit rotations with the c-Phase gates, we produce entangled states with high fidelity to the Bell states, $|\Psi_\pm\rangle = (|0,0\rangle \pm |1,1\rangle)/\sqrt{2}$ and $|\Phi_\pm\rangle = (|1,0\rangle \pm |0,1\rangle)/\sqrt{2}$, where $|l,r\rangle$ denotes excitation level $l(r)$ of the left (right) qubit [21].

To accurately and precisely detect this two-qubit entanglement, we seek a complete physical model and calibration of the joint readout. The physical mechanism enabling the joint readout is a qubit-state-dependent dispersive cavity shift that is large relative to the cavity linewidth $\kappa/2\pi = 1$ MHz. In this strong dispersive regime [22,23], the system is described by a dispersive Jaynes-Cummings Hamiltonian ($\hbar = 1$)

$$H_{\mathrm{JC}} = (\omega_{\mathrm{C}} + \chi^{\mathrm{L}} ZI + \chi^{\mathrm{R}} IZ)a^\dagger a - \frac{\omega^{\mathrm{L}}}{2} ZI - \frac{\omega^{\mathrm{R}}}{2} IZ, \quad (1)$$

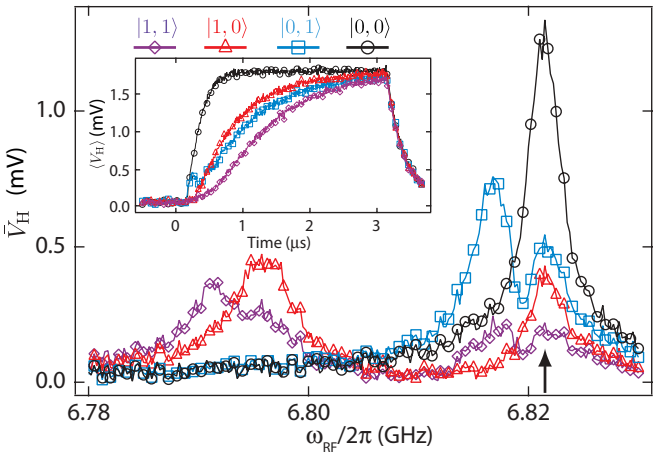

FIG. 1. (Color online) Time average of a pulsed cavity transmission versus drive frequency having prepared the four computational basis states $|0,0\rangle$ (circles), $|0,1\rangle$ (squares), $|1,0\rangle$ (triangles), $|1,1\rangle$ (diamonds), demonstrating the four dispersive cavity peaks. Inset: Measured pulse transients of V_{H} at the transmission frequency corresponding to $|0,0\rangle$ (indicated by black arrow) for the same four prepared states. Measurement is pulsed on at 0 μs for a duration of 3 μs.

where ω_{C} is the bare resonator frequency, $\omega^{\mathrm{L(R)}}$ is the ground to first excited state transition frequency for the left (right) qubit, and $\chi^{\mathrm{L(R)}}$ is the left (right) qubit-state-dependent cavity shift. To determine the qubit-dependent shifts we prepare each of the four computational basis states ($|0,0\rangle$, $|0,1\rangle$, $|1,0\rangle$, $|1,1\rangle$) using single-qubit gates, and we measure the transmitted voltage. Figure 1 shows the time-averaged homodyne voltage $\bar{V}_{\mathrm{H}} = \langle \int_0^{\Delta t} V_{\mathrm{H}} dt \rangle / \Delta t$, where $\Delta t = 0.5$ μs. As expected, we find four peaks corresponding to the four computational states and estimate from their separation $\chi^{\mathrm{L(R)}}/2\pi = 13(4)$ MHz.

When the shifts are many linewidths ($\chi^{\mathrm{L}}, \chi^{\mathrm{R}} \gg \kappa$) and qubit relaxation during measurement is negligible ($\Delta t \ll T_1$), driving with a tone at the cavity frequency corresponding to $|0,0\rangle$ would query the joint property that *both qubits are in the ground state*: Transmission is high when the state is projected onto $|0,0\rangle$ and zero otherwise. In this ideal scenario, $\bar{V}_{\mathrm{H}} = \mathrm{Tr}(\rho M)$, where ρ is the two-qubit density matrix and $M \propto |0,0\rangle\langle 0,0| = (I + ZI + IZ + ZZ)/4$ is the measurement operator. However, qubit relaxation during the measurement and partial overlap of the dispersive peaks, evident in the inset of Fig. 1, make the measurement operator take the more general form

$$M = \beta_{II} II + \beta_{ZI} ZI + \beta_{IZ} IZ + \beta_{ZZ} ZZ, \qquad (2)$$

where $\{\beta_{LR}\}$ are constants that must be calibrated.

This same technique can be extended to a circuit QED system with three or four transmon qubits by putting two at each end of the cavity [24]. In principle, this can be extended to a larger number, although that has yet to be investigated.

B. Verification of the model

A comprehensive test of this measurement model is performed with a sequence of Rabi-flopping experiments. Figures 2(a) and 2(b) show $\bar{V}_{\mathrm{H}}$ as a function of the duration

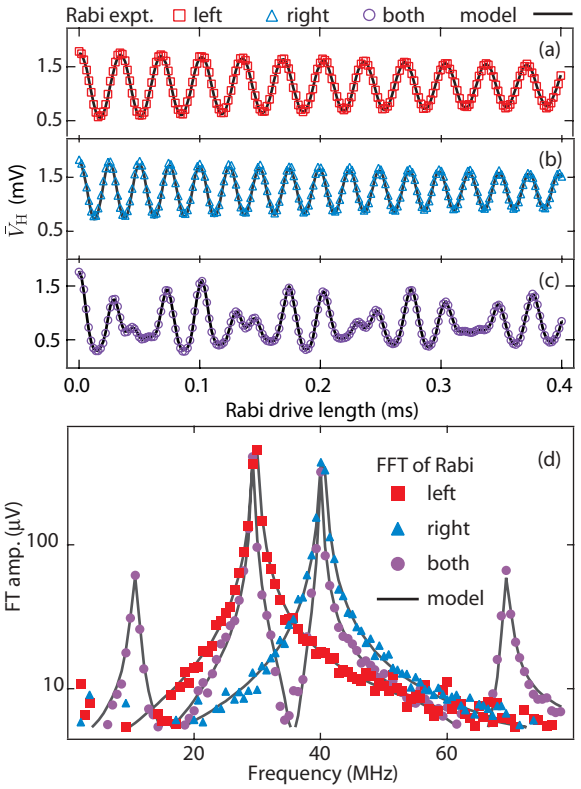

FIG. 2. (Color online) Rabi oscillations on (a) the left qubit, (b) the right qubit, and (c) simultaneously on both. Solid lines are fits to the model in Eq. (3). (d) Fourier transform (FT) of the three Rabi experiments (circles) and of best fits (lines). While the red (blue) traces show one main peak at the Rabi frequency $\Omega^{\mathrm{L(R)}}$, the purple traces reveal peaks at Ω^{L}, Ω^{R}, $\Omega^{\mathrm{L}} + \Omega^{\mathrm{R}}$, and $\Omega^{\mathrm{L}} - \Omega^{\mathrm{R}}$, demonstrating the mixing property that makes the joint measurement sensitive to qubit-qubit correlations.

of an applied drive at ω^{L} and ω^{R}, respectively. In each case the drive induces a Rabi oscillation of the addressed qubit around the y axis of its Bloch sphere. By varying the strength of the drive at either frequency, we can have different Rabi frequencies on each qubit. We fit these oscillations using the most general two-qubit measurement operator

$$M = \sum_{L,R \in \{I,X,Y,Z\}} \beta_{LR} LR, \qquad (3)$$

with theoretical expressions for $\langle Z \rangle$ and $\langle X \rangle$ assuming independently driven qubits (see Appendix C). The best fits place bounds on deviations from Eq. (2) due to undesired terms such as $\langle XI \rangle$ ($\langle IX \rangle$) and $\langle XZ \rangle$ ($\langle ZX \rangle$) to $\lesssim 2\%$ of the full range of $\bar{V}_{\mathrm{H}}$ each.

A third experiment, shown in Fig. 2(c), measures $\bar{V}_{\mathrm{H}}$ in response to simultaneous driving of both qubits. There are frequency components at the individual qubit Rabi frequencies, Ω^{L} and Ω^{R}, but also at the sum and difference due to the ZZ term in Eq. (2). This is clearly revealed in the Fourier transform of the oscillations shown in Fig. 2(d). Fitting with the measurement model of Eq. (3), we find deviations from Eq. (2) due to the undesired correlation $\langle XX \rangle$ term to be less than 2% of the peak-to-peak excursion of $\langle \bar{V}_{\mathrm{H}} \rangle$ (see Appendix C). These Rabi experiments thus corroborate Eq. (2) and give the

calibration $(\beta_{II},\beta_{IZ},\beta_{ZI},\beta_{ZZ}) = (800, 380, 380, 200)\ \mu$V. The jointness, which we define as $\beta_{ZZ}/\beta_{IZ(ZI)}$, is 0.6, indicating the high sensitivity to two-qubit correlations.

III. STATE TOMOGRAPHY OF HIGHLY ENTANGLED STATES

Having characterized the joint readout, we can now perform quantum state tomography of separable and entangled two-qubit states. We extend Ref. [12], where two-qubit state tomography with a joint readout was first demonstrated, by obtaining an overcomplete set of 30 measurements through applying different pairs of simultaneous single-qubit rotations prior to detection (see Appendix D). Using linear least-squares estimation, we then extract the Pauli set $\vec{P}$, whose 16 elements are the expectation values of the two-qubit Pauli operators, $\langle LR\rangle$, where $L,R \in \{I,X,Y,Z\}$. The two-qubit density matrix is linearly related to the elements of $\vec{P}$ by $\rho = \sum_{L,R} LR\langle LR\rangle/4$.

An advantage of examining the set $\vec{P}$ is that it is a simple visual tool to distinguish separable from entangled states. In Fig. 3, we show two separable and two entangled states. For these states, $\vec{P}$ ideally contains three nonzero bars, all of unit magnitude. $\vec{P}$ can be divided into three sections: the single-qubit polarization vectors, $\vec{P}^{\rm L} = \{XI,YI,ZI\}$ (red) and $\vec{P}^{\rm R} = \{IX,IY,IZ\}$ (blue), and the vector of two-qubit correlations $\vec{Q} = \{\langle XY\rangle,\ldots,\langle ZZ\rangle\}$ (purple). For the separable states, we observe near-unity components in each of the three sections. In contrast, for the entangled states, only $\vec{Q}$ has components with near-unity magnitude. The presence of strong correlations and vanishing qubit polarization is a signature of a high degree of entanglement.

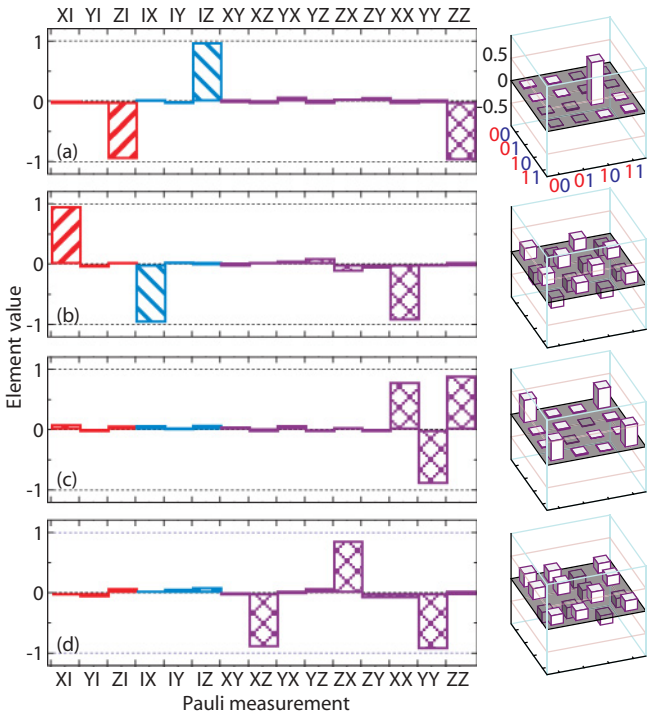

FIG. 3. (Color online) Experimental Pauli set (with trivial $\langle II\rangle = 1$ not shown), for separable states (a) $|1,0\rangle$ and (b) $(|0,0\rangle - |0,1\rangle + |1,0\rangle - |1,1\rangle)/2$ and entangled states (c) $|\Psi_+\rangle$ and (d) $(|0,0\rangle + |0,1\rangle - |1,0\rangle + |1,1\rangle)/2$. Upward-angling (downward-angling) bars correspond to left (right) single-qubit Pauli operators. Crossed bars are the qubit-qubit correlations. The fidelities to the four targeted states are $\mathcal{F} = 98.2\% \pm 0.4\%$, $96.8\% \pm 0.4\%$, $90.0\% \pm 0.6\%$, and $92.5\% \pm 0.7\%$. The real part of the density matrix obtained using the constrained maximum-likelihood estimation on the same raw measurements is shown in the plot to the right of each Pauli set.

IV. ENTANGLEMENT WITNESSES

Finally, we use the calibrated joint readout to measure the fidelity to targeted states and characterize the entanglement via entanglement witnesses including CHSH operators. The fidelity $\mathcal{F} = \langle\Psi|\rho|\Psi\rangle$ to a targeted state $|\Psi\rangle$ quantifies the control over two-qubit states, and it is given by $\mathcal{F} = (\vec{P}\cdot\vec{P}_{\rm target})/4$. We define two experiments, involving a rotation θ of the left qubit about its y axis having prepared the separable state $|0,0\rangle$ [experiment I, Fig. 4(a)] and the entangled state $(|0,0\rangle + |0,1\rangle - |1,0\rangle + |1,1\rangle)/2$ [experiment II, Fig. 4(b)]. For experiments I and II, we find $\mathcal{F} = 98.8\% \pm 1.0\%$ and $93.4\% \pm 1.5\%$ (averaged over θ), respectively. We find excellent agreement between experiment and simulation, demonstrating the accuracy of both the state preparation and the measurement.

Measures beyond fidelity are necessary to quantify the degree of two-qubit entanglement. Often, entanglement monotones such as concurrence $\mathcal{C}$ [25] are obtained using nonlinear estimators. It is standard to first perform maximum-likelihood estimation [26] to generate a positive ρ despite statistical or systematic errors in the measurements, and to then calculate these metrics from the eigenvalue spectrum of related matrices [25]. This nonlinear process greatly complicates the propagation of any statistical and systematic errors in the measurements. It can also bias the estimation of metrics such as $\mathcal{C}$ when the purity of the two-qubit state is high compared to the readout fidelity [27,28] (see Appendix F), as is typically the case with superconducting qubits.

To make quantitative statements about entanglement while using only linear operations on measurements, we make use of entanglement witnesses [25,29]. An entanglement witness $\mathcal{W}$ is a unity-trace observable with a positive expectation value for all separable states, such that $\mathrm{Tr}(\rho\mathcal{W}) < 0$ guarantees entanglement. Furthermore, $\mathcal{B} = -2\mathrm{Tr}(\rho\mathcal{W})$ gives a lower bound [29] on $\mathcal{C}$. The optimal witnesses (strictest lower bound) for the Bell states are

$$\mathcal{W}_{\Psi\pm} = \tfrac{1}{4}(II \mp XX \pm YY - ZZ),$$
$$\mathcal{W}_{\Phi\pm} = \tfrac{1}{4}(II \mp XX \mp YY + ZZ).$$

The measured bounds for experiments I and II are shown in Figs. 4(c) and 4(d). In experiment I, the four bounds are nonpositive for all θ to within measurement error, indicating that entanglement is not witnessed. This is expected, since single-qubit rotations should not produce any entanglement. In Fig. 4(d), in contrast, bounds $\mathcal{B}_{\Psi+}$ and $\mathcal{B}_{\Phi-}$ extend into the positive region, reaching $85.9\% \pm 1.5\%$ and $88.1\% \pm 1.5\%$ at $\theta = -90^\circ$ and 90°, respectively. There is at least one positive

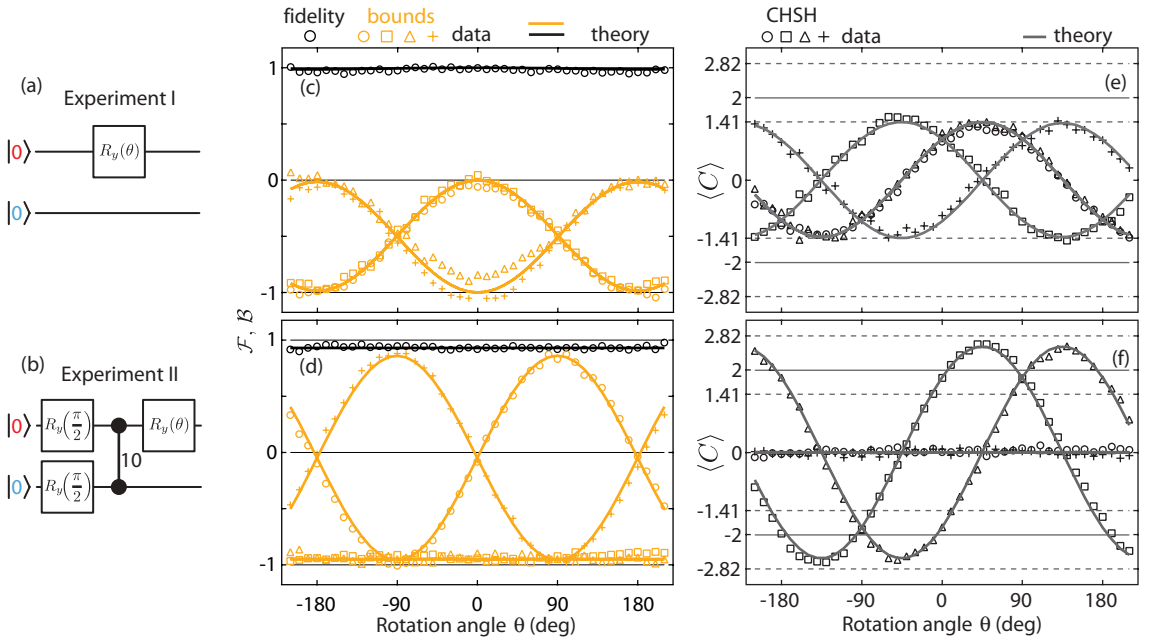

FIG. 4. (Color online) Pulse sequences for a collection of (a) separable and (b) entangled states, showing experimental lower bounds $\mathcal{B}_i$ (orange) on concurrence given by the optimal witnesses for Bell states $\mathcal{W}_{\Psi+}$ (circles), $\mathcal{W}_{\Psi-}$ (squares), $\mathcal{W}_{\Phi+}$ (triangles), and $\mathcal{W}_{\Phi-}$ (crosses), and fidelity $\mathcal{F}$ to the ideal state (black circles) for (c) experiment I and (d) experiment II. In (d), a maximum lower bound is reached by $\mathcal{B}_{\Phi-}$ ($\mathcal{B}_{\Psi+}$) at $\theta = -90°(+90)°$. Shown are four measured CHSH operators, $\langle C_{ZXXZ}\rangle$ (squares), $\langle C_{ZXZX}\rangle$ (triangles), $\langle C_{ZZXX}\rangle$ (circles), and $\langle C_{XXZZ}\rangle$ (crosses), for a collection of (e) separable and (f) entangled states. Experiment I in (e) involves only a single qubit rotation and all $\langle C\rangle$ values stay within the separable state bounds $\pm\sqrt{2}$ up to measurement noise. For experiment II in (f), there are three single-qubit rotations and a c-Phase, and we find max $|\langle C\rangle| = 2.61 \pm 0.04$. Solid curves are the results of master equation simulations.

bound for most θ (excluding $\pm 180°$ and $0°$), indicating that the two qubits are entangled. Agreement with the master equation simulation (solid lines) in Figs. 4(c) and 4(d) shows the accuracy of the entanglement witnesses and the small residuals ($\sim$2%) demonstrate the precision of measurement by joint readout.

Although the CHSH operator is often used to test quantum mechanics against local-hidden variable (LHV) theories, here we can also employ it as an entanglement witness [29]. A CHSH operator [16] is defined as

$$C_{L,R,L',R'} = LR + LR' + L'R - L'R', \tag{4}$$

with $\{L, L'\}$ and $\{R, R'\}$ being pairs of single-qubit Pauli operators along any two axes of the left and right qubits, respectively. With a general choice of axes, for separable states, $|\langle C\rangle| \leqslant 2$, coinciding with the LHV bound. For the specific choice $L \perp L'$ and $R \perp R'$, the separable bound is tighter, $|\langle C\rangle| \leqslant \sqrt{2}$.

From a subset of the measured $\vec{P}$ for states generated in experiments I and II, we obtain expectation values of four CHSH operators with $L, L' \in \{X^{\mathrm{L}}, Z^{\mathrm{L}}\}$ and $R, R' \in \{X^{\mathrm{R}}, Z^{\mathrm{R}}\}$. For experiment I, shown in Fig. 4(c), we find to within statistical error (standard deviation of 0.04) that $\langle C_{ZXXZ}\rangle = \langle XX\rangle - \langle XZ\rangle + \langle ZX\rangle + \langle ZZ\rangle$ (squares) and $\langle C_{ZXZX}\rangle = \langle XX\rangle + \langle XZ\rangle - \langle ZX\rangle + \langle ZZ\rangle$ (triangles) remain within one standard deviation of the separable bound for all θ. Conversely, for the entangled states prepared in experiment II, shown in Fig. 4(d), $\langle C\rangle$ clearly oscillates well past the separable bounds. At $\theta = \pm 45°$, a maximum value $|\langle C\rangle| = 2.61 \pm 0.04$ is reached. The agreement with theory and proximity of this maximum $|\langle C\rangle|$ to the $2\sqrt{2}$ upper bound [30] at angles very close to the expected $\pm 45°$ further demonstrate the highly entangled states produced and the ability of the joint measurement to determine the degree of entanglement precisely. Here, $|\langle C\rangle|$ exceeds the separable state bound of $\sqrt{2}$ by $\sim$30 standard deviations. Furthermore, it also violates a Bell inequality by exceeding the classical bound of 2 by $\sim$15 standard deviations. Locality and detection loopholes present in our system preclude a fundamental test disproving LHV. For Josephson phase qubits, the detection loophole has recently been closed using independent single-shot readouts [7]. We emphasize that we calibrate the measurement and the gates but we do not specifically optimize for a maximum $\langle C\rangle$ value.

V. CONCLUSION

In summary, we have demonstrated a joint readout of superconducting qubits using a microwave cavity as a single measurement channel that gives direct access to qubit correlations. This readout is advantageous because it introduces the minimal number of channels for qubit decoherence and is easy to model and calibrate accurately. The joint readout represents a different strategy from that of individual qubit readouts, but it is shown to be a viable approach for precisely characterizing entangled states. Applying this readout to analyze highly entangled states, we report a large violation of CHSH inequalities in a solid-state system. These results represent an advance in the ability to quantify the entanglement between qubits. In its present form, this joint readout has the

resolution to detect future improvements in two-qubit gates and has already been extended to a circuit QED system with up to four qubits [24], where it has been used to detect three-qubit entangled states such as the Greenberger-Horne-Zeilinger state. Furthermore, the possibility of measuring multiqubit parity operators in three- to four-qubit systems could be useful for performing quantum error correction protocols [31], generating entanglement by postselection [32,33], or performing fundamental tests of quantum contextuality [34,35].

ACKNOWLEDGMENTS

We acknowledge discussions with R. Blume-Kohout, B. R. Johnson, Jens Koch, N. Lütkenhaus, K. Resch, C. Rigetti, and D. I. Schuster. This work was supported by LPS/NSA under ARO Contract No. W911NF-05-1-0365 and by the NSF under Grant Nos. DMR-0653377 and DMR-0603369. Additional support is acknowledged from CIFAR, MITACS, MRI, and NSERC (JMG) and from CNR-Istituto di Cibernetica, Pozzuoli, Italy (LF).

APPENDIX A: SAMPLE FABRICATION

The device is fabricated on a 430-μm-thick sapphire substrate. The superconducting transmission-line cavity and flux-bias lines are defined via optical lithography and fluorine-based reactive ion etching of a dcsputtered niobium film (180 nm thick). The two transmons are patterned using electron-beam lithography with split junctions, grown using double-angle deposition of aluminium, with bottom and top layer thicknesses of 20 and 80 nm, respectively. The sample is cooled in a dilution refrigerator to 13 mK. A basic schematic is shown here in Fig. 5. Full details of the setup are presented in a previous publication [21].

APPENDIX B: EXPERIMENTAL DEVICE PARAMETERS

From a set of transmission measurements obtained when tuning each qubit into near resonance with the cavity, we determine the qubit-cavity coupling strengths $g_{\mathrm{L(R)}}/2\pi =$ 199 (183) MHz. Fitting a multilevel Jaynes-Cummings Hamiltonian to spectroscopy measurements of the two lowest transitions of each qubit, we extract maximum Josephson

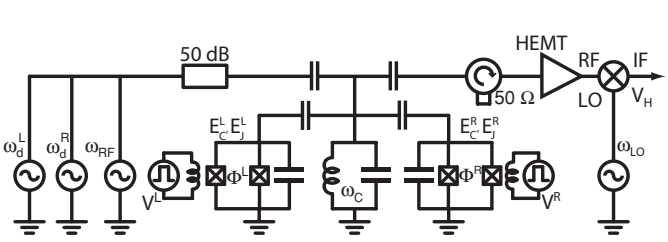

FIG. 5. Circuit diagram of experimental setup, showing the cavity as a lumped LC resonator. Microwave drive tones that address the cavity, ω_{RF}, and qubits, $\omega_{\mathrm{d}}^{\mathrm{L(R)}}$, are applied via the cavity input line. The left (right) qubit, with Josephson energy $E_J^{\mathrm{L(R)}}$ and charging energy $E_C^{\mathrm{L(R)}}$, is tunable via a local flux $\Phi^{\mathrm{L(R)}}$ set by a voltage $V^{\mathrm{L(R)}}$. The joint qubit state information is transmitted out a single readout line, amplified through a high electron mobility transistor (HEMT) amplifier at 4 K and mixed down at room temperature for digital processing.

energies $E_{\mathrm{J,L(R)}}^{\max}/h = 28.48$ (42.34) GHz and electrostatic charging energies $E_{\mathrm{C,L(R)}}/h = 317$ (297) MHz. Sliding π-pulse and Ramsey fringe experiments give qubit relaxation times $T_1^{\mathrm{L(R)}} = 1.2$ (0.9) μs and dephasing times $T_2^{\mathrm{L(R)}} =$ 1.5 (1.1) μs.

APPENDIX C: MEASUREMENT MODEL VALIDATION

As mentioned in the main text, we fit the three Rabi-flopping experiments of Fig. 2 to place bounds on deviations from the measurement model of Eq. (2). Because in these tests each qubit is driven around the y axis of its Bloch sphere, all terms involving Y^{L} and Y^{R} in Eq. (3) would not contribute to $\bar{V}_{\mathrm{H}}$. The presence of such terms can be tested by rotating each or both qubits around their x axis instead. We do not find any significant differences in such experiments from the ones presented in the text, and the results here can be generalized for both quadratures.

In our experiment the detuning of $\sim$1.5 GHz between the two qubits is large compared to the Rabi-flopping rates, and we can assume a simple model of independent qubit driving. For a qubit driven at a rate Ω around its y axis starting from the ground state, the theoretical time evolution of $\langle Z\rangle$ and $\langle X\rangle$ is given by

$$\langle Z\rangle(t) = \frac{\gamma_1\gamma_2}{\gamma_1\gamma_2+\Omega^2} + \frac{e^{-t/\tau_R}\Omega^2}{\gamma_1\gamma_2+\Omega^2}\left(\cos(\tilde{\Omega}t) + \frac{\sin(\tilde{\Omega}t)}{\tau_R\tilde{\Omega}}\right),$$

$$\langle X\rangle(t) = \frac{\gamma_1\Omega}{\gamma_1\gamma_2+\Omega^2} - \frac{e^{-t/\tau_R}\Omega}{\gamma_1\gamma_2+\Omega^2} \times\left(\gamma_1\cos(\tilde{\Omega}t) - \frac{[2\Omega^2+\gamma_1(\gamma_2-\gamma_1)]\sin(\tilde{\Omega}t)}{2\tilde{\Omega}}\right).$$

Here, $\tilde{\Omega} = \sqrt{\Omega^2-(1/\tau_R)^2}$ is an effective oscillation rate, $\gamma_1 = 1/T_1$ is the relaxation rate, $\gamma_2 = \gamma_1/2+\gamma_\phi$ is the dephasing rate, and $\tau_R = 2/(\gamma_1+\gamma_2)$ is the Rabi decay time.

Using these expressions in the full model, Eq. (3), and fitting to the three experimental curves, we estimate the coefficients β_{LR}. For single-qubit driving [Fig. 2(a)], the right qubit is always in the ground state, and only terms $\langle ZI\rangle$, $\langle XI\rangle$, $\langle XZ\rangle$, and $\langle ZZ\rangle$ contribute to the $\bar{V}_{\mathrm{H}}$ oscillation. Similarly, for Fig. 2(b), with the left qubit in the ground state, only terms $\langle IZ\rangle$, $\langle IX\rangle$, $\langle ZX\rangle$, and $\langle ZZ\rangle$ contribute. Using the functions

$$\bar{V}_{\mathrm{H}}^a = W_0 + W_1\langle ZI\rangle + W_2\langle XI\rangle,$$
$$\bar{V}_{\mathrm{H}}^b = W_0 + W_1\langle IZ\rangle + W_2\langle IX\rangle,$$

with free parameters W_0, W_1, W_2, $\Omega^{\mathrm{L(R)}}$, $\gamma_1^{\mathrm{L(R)}}$, and $\gamma_2^{\mathrm{L(R)}}$, gives an excellent best fit. In both cases, the best-fit W_2, corresponding to $\beta_{XI(IX)}+\beta_{XZ(ZX)}$, is less than 2% of the full range of $\bar{V}_{\mathrm{H}}$, $\sim 2\beta_{IZ}+2\beta_{ZI}$. For the doubly-driven case [Fig. 2(c)], the fit function used is

$$\bar{V}_{\mathrm{H}}^c = \beta_{II} + \beta_{XI}\langle XI\rangle + \beta_{ZI}\langle ZI\rangle + \beta_{IX}\langle IX\rangle + \beta_{IZ}\langle IZ\rangle + \beta_{XX}\langle XX\rangle + \beta_{XZ}\langle XZ\rangle + \beta_{ZX}\langle ZX\rangle + \beta_{ZZ}\langle ZZ\rangle,$$

with β_{ij}, Ω^{L}, Ω^{R}, γ_j^{L}, and γ_j^{R} as fit parameters. The best-fit coefficients captured in Eq. (2) are $(\beta_{II},\beta_{IZ},\beta_{ZI},\beta_{ZZ}) =$ (800, 380, 380, 200) μV. Best-fit values of the remaining coefficients are each less than 2% of the full range of $\bar{V}_{\mathrm{H}}$.

TABLE I. The 30 raw measurements.

	Prerotation	Measurement operator
M_{01}	$I \otimes I$	$+\beta_{ZI} ZI + \beta_{IZ} IZ + \beta_{ZZ} ZZ$
M_{02}	$R_x^{\pi} \otimes I$	$-\beta_{ZI} ZI + \beta_{IZ} IZ - \beta_{ZZ} ZZ$
M_{03}	$I \otimes R_x^{\pi}$	$+\beta_{ZI} ZI - \beta_{IZ} IZ - \beta_{ZZ} ZZ$
M_{04}	$R_x^{\pi/2} \otimes I$	$+\beta_{ZI} YI + \beta_{IZ} IZ + \beta_{ZZ} YZ$
M_{05}	$R_x^{\pi/2} \otimes R_x^{\pi/2}$	$+\beta_{ZI} YI + \beta_{IZ} IY + \beta_{ZZ} YY$
M_{06}	$R_x^{\pi/2} \otimes R_y^{\pi/2}$	$+\beta_{ZI} YI - \beta_{IZ} IX - \beta_{ZZ} YX$
M_{07}	$R_x^{\pi/2} \otimes R_x^{\pi}$	$+\beta_{ZI} YI - \beta_{IZ} IZ - \beta_{ZZ} YZ$
M_{08}	$R_y^{\pi/2} \otimes I$	$-\beta_{ZI} XI + \beta_{IZ} IZ - \beta_{ZZ} XZ$
M_{09}	$R_y^{\pi/2} \otimes R_x^{\pi/2}$	$-\beta_{ZI} XI + \beta_{IZ} IY - \beta_{ZZ} XY$
M_{10}	$R_y^{\pi/2} \otimes R_y^{\pi/2}$	$-\beta_{ZI} XI - \beta_{IZ} IX + \beta_{ZZ} XX$
M_{11}	$R_y^{\pi/2} \otimes R_x^{\pi}$	$-\beta_{ZI} XI - \beta_{IZ} IZ + \beta_{ZZ} XZ$
M_{12}	$I \otimes R_x^{\pi/2}$	$+\beta_{ZI} ZI + \beta_{IZ} IY + \beta_{ZZ} ZY$
M_{13}	$R_x^{\pi} \otimes R_x^{\pi/2}$	$-\beta_{ZI} ZI + \beta_{IZ} IY - \beta_{ZZ} ZY$
M_{14}	$I \otimes R_y^{\pi/2}$	$+\beta_{ZI} ZI - \beta_{IZ} IX - \beta_{ZZ} ZX$
M_{15}	$R_x^{\pi} \otimes R_y^{\pi/2}$	$-\beta_{ZI} ZI - \beta_{IZ} IX + \beta_{ZZ} ZX$
N_{01}	$I \otimes I$	$+\beta_{ZI} ZI + \beta_{IZ} IZ + \beta_{ZZ} ZZ$
N_{02}	$R_x^{-\pi} \otimes I$	$-\beta_{ZI} ZI + \beta_{IZ} IZ - \beta_{ZZ} ZZ$
N_{03}	$I \otimes R_x^{-\pi}$	$+\beta_{ZI} ZI - \beta_{IZ} IZ - \beta_{ZZ} ZZ$
N_{04}	$R_x^{-\pi/2} \otimes I$	$-\beta_{ZI} YI + \beta_{IZ} IZ - \beta_{ZZ} YZ$
N_{05}	$R_x^{-\pi/2} \otimes R_x^{-\pi/2}$	$-\beta_{ZI} YI - \beta_{IZ} IY + \beta_{ZZ} YY$
N_{06}	$R_x^{-\pi/2} \otimes R_y^{-\pi/2}$	$-\beta_{ZI} YI + \beta_{IZ} IX - \beta_{ZZ} YX$
N_{07}	$R_x^{-\pi/2} \otimes R_x^{-\pi}$	$-\beta_{ZI} YI - \beta_{IZ} IZ + \beta_{ZZ} YZ$
N_{08}	$R_y^{-\pi/2} \otimes I$	$+\beta_{ZI} XI + \beta_{IZ} IZ + \beta_{ZZ} XZ$
N_{09}	$R_y^{-\pi/2} \otimes R_x^{-\pi/2}$	$+\beta_{ZI} XI - \beta_{IZ} IY - \beta_{ZZ} XY$
N_{10}	$R_y^{-\pi/2} \otimes R_x^{-\pi/2}$	$+\beta_{ZI} XI + \beta_{IZ} IX + \beta_{ZZ} XX$
N_{11}	$R_y^{-\pi/2} \otimes R_x^{-\pi}$	$+\beta_{ZI} XI - \beta_{IZ} IZ - \beta_{ZZ} XZ$
N_{12}	$I \otimes R_x^{-\pi/2}$	$+\beta_{ZI} ZI - \beta_{IZ} IY - \beta_{ZZ} ZY$
N_{13}	$R_x^{-\pi} \otimes R_x^{-\pi/2}$	$-\beta_{ZI} ZI - \beta_{IZ} IY + \beta_{ZZ} ZY$
N_{14}	$I \otimes R_y^{-\pi/2}$	$+\beta_{ZI} ZI + \beta_{IZ} IX + \beta_{ZZ} ZX$
N_{15}	$R_x^{-\pi} \otimes R_y^{-\pi/2}$	$-\beta_{ZI} ZI + \beta_{IZ} IX - \beta_{ZZ} ZX$

APPENDIX D: TWO-QUBIT STATE TOMOGRAPHY

Full tomography of the two-qubit state is performed similarly to what was done in Ref. [12], but using an overcomplete set of 30 raw measurements. These measurements involve applying different simultaneous rotations on the qubits, as listed in Table I. The 15 measurements labeled M_i involve positive rotations chosen from $\{I, R_x^{+\pi}, R_x^{+\pi/2}, R_y^{+\pi/2}\}$. The remaining 15, labeled N_i, involve negative rotations chosen from $\{I, R_x^{-\pi}, R_x^{-\pi/2}, R_y^{-\pi/2}\}$. Ensemble averages of M_i and N_i are obtained by repeating state preparation, analysis rotation, and measurement 600,000 times. A linear least-squares estimator is then used to extract the Pauli set $\vec{P}$ discussed in the text. Although just 15 linearly independent measurements (such as either all M_i or all N_i) are sufficient for state tomography, using all of these rotations and least-squares estimation reduces the statistical and systematic error in the extraction of $\vec{P}$.

APPENDIX E: SYSTEMATIC ERRORS

To test for systematic errors we measure $\vec{P}$ for a collection of states that differ only by a single-qubit rotation prior to measurement. These errors in detection could appear as offsets or amplitudes that exceed the ± 1 range of the elements of

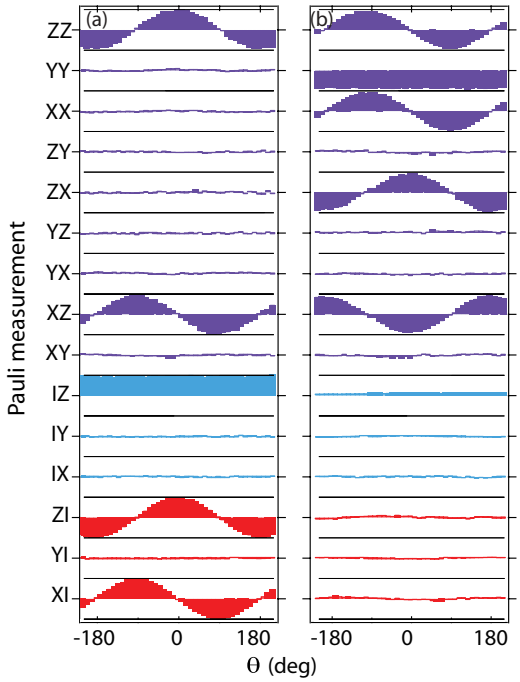

FIG. 6. (Color online) Evolution of the Pauli set $\vec{P}$ for experiments I and II given in the main text. (a) For experiment I, the left qubit polarization rotates along the x-z plane, while the right qubit remains fully polarized along z. (b) For experiment II, both qubit polarizations vanish, with the only nonzero and oscillating Pauli operators being qubit-qubit correlators (purple bars).

$\vec{P}$. We can investigate each of the individual components of $\vec{P}$ for experiment I [Fig. 4(a)] and experiment II [Fig. 4(b)] described in the main text. In experiment I, $\langle XI \rangle$, $\langle ZI \rangle$, $\langle XZ \rangle$, and $\langle ZZ \rangle$ oscillate with an average visibility of $97.6 \pm 0.3\%$ [Fig. 6(a)]. Moreover, the measured amplitude of all the ideally zero bars is less than 0.1. In experiment II, the dominant oscillating components are all in $\vec{Q}$ [Fig. 6(b)], indicating that the state remains entangled throughout. In this case, we find a visibility of $91.5\% \pm 0.3\%$, in good agreement with a master equation simulation incorporating qubit relaxation and dephasing. An oscillation amplitude of $\sim$0.1 is observed in $\langle XI \rangle$ and $\langle ZI \rangle$, a factor $\sim$2 larger than expected from theory.

There are a variety of higher order and systematic effects that can affect the accuracy of the entanglement detection at the few-percent level and explain the discrepancies in some of the terms of Fig. 6(b). One possible effect is a systematic under-rotation of both qubits by 1%. There are also higher order couplings that are relevant at this level. The first is the finite strength of the two-qubit ZZ entangling interaction [21] even in the off state ($\zeta/2\pi \sim 1.2$ MHz). This residual coupling leads to errors in some of the two-qubit correlation terms on the order of $\zeta/\Omega^{\mathrm{L(R)}} \sim 2\%$. A second is the presence of a residual qubit-qubit interaction [11] ($J/2\pi \sim 60$ MHz), which can lead to errors of order $J/(\omega^{\mathrm{L}} - \omega^{\mathrm{R}}) \sim 4\%$. Another effect is the qubit-state-dependent filtering of the drive applied to a qubit, which is expected to be on the order of $\chi^{\mathrm{R(L)}}/(\omega^{\mathrm{L(R)}} - \omega_{\mathrm{C}}) \sim 2\%$. The effect of these couplings can be mitigated by

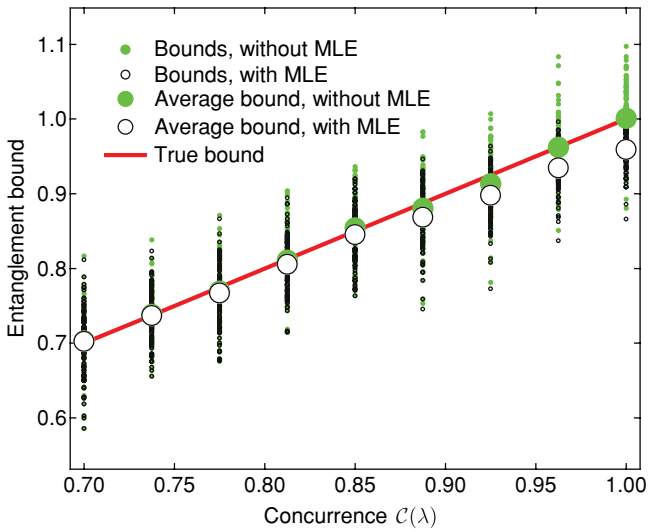

FIG. 7. (Color online) Biasing of entanglement bounds by maximum-likelihood estimation, showing comparison of the lower bound $\mathcal{B}_{\psi-}$ on concurrence $\mathcal{C}$ computed from simulated noisy raw data with and without use of MLEs. The bound computed using MLEs systematically underestimates the true bound (in this case, always equal to the true concurrence $\mathcal{C}$, red line), while the bound computed directly from the simulated raw data remains faithful even as the Werner state approaches the Bell state $|\Psi^-\rangle$ (i.e., as $\lambda \to 1$). For $|\Psi^-\rangle$, the MLE-computed bound underestimates the true bound by 4%.

implementing appropriate composite pulse schemes [36] and will be explored in the future.

APPENDIX F: BIASING OF METRICS BY MAXIMUM-LIKELIHOOD ESTIMATION

Maximum-likelihood estimators (MLEs) can become biased if the true mean lies close to a boundary of the allowed parameter space [37]. In order to quantify the importance of this effect on the estimation of lower bounds on concurrence $\mathcal{C}$ given by entanglement witnesses, we have performed Monte Carlo simulations for nearly pure Werner states [25],

$$\rho_W(\lambda) = \lambda|\psi^-\rangle\langle\psi^-| + (1-\lambda)I/4,$$

with Werner parameter $\lambda \in [0.8, 1]$.

We have created 100 sets of simulated raw measuremens ftor each λ by assuming Gaussian amplifier noise consistent with the experiment. Figure 7 shows the concurrence bound $\mathcal{B}_{\psi-}$ as a function of the true $\mathcal{C}$ of the Werner state, obtained with and without MLE processing of the simulated noisy data. We find that while the mean of $\mathcal{B}_{\psi-}$ estimated directly from the raw data is unbiased, the mean of the concurrence bound obtained with MLEs becomes increasingly biased the more pure the Werner state becomes (i.e., the closer λ is to unity). MLEs underestimate the bound by 1% at $\mathcal{C} = 0.85$ and by 4% at $\mathcal{C} = 1$.

[1] A. H. Myerson, D. J. Szwer, S. C. Webster, D. T. C. Allcock, M. J. Curtis, G. Imreh, J. A. Sherman, D. N. Stacey, A. M. Steane, and D. M. Lucas, Phys. Rev. Lett. **100**, 200502 (2008).

[2] H. Haffner *et al.*, Nature (London) **438**, 643 (2005).

[3] D. Leibfried *et al.*, Nature (London) **438**, 639 (2005).

[4] E. Lucero, M. Hofheinz, M. Ansmann, R. C. Bialczak, N. Katz, M. Neeley, A. D. O'Connell, H. Wang, A. N. Cleland, and J. M. Martinis, Phys. Rev. Lett. **100**, 247001 (2008).

[5] J. M. Chow, J. M. Gambetta, L. Tornberg, J. Koch, L. S. Bishop, A. A. Houck, B. R. Johnson, L. Frunzio, S. M. Girvin, and R. J. Schoelkopf, Phys. Rev. Lett. **102**, 090502 (2009).

[6] R. McDermott, R. W. Simmonds, M. Steffen, K. B. Cooper, K. Cicak, K. D. Osborn, S. Oh, D. P. Pappas, and J. M. Martinis, Science **307**, 1299 (2005).

[7] M. Ansmann *et al.*, Nature (London) **461**, 504 (2009).

[8] F. Mallet, F. R. Ong, A. Palacios-Laloy, F. Nguyen, P. Bertet, D. Vion, and D. Esteve, Nature Phys. **5**, 791 (2009).

[9] W. Mao, D. V. Averin, R. Ruskov, and A. N. Korotkov, Phys. Rev. Lett. **93**, 056803 (2004).

[10] B. Trauzettel, A. N. Jordan, C. W. J. Beenakker, and M. Büttiker, Phys. Rev. B **73**, 235331 (2006).

[11] J. Majer *et al.*, Nature (London) **449**, 443 (2007).

[12] S. Filipp *et al.*, Phys. Rev. Lett. **102**, 200402 (2009).

[13] A. Wallraff, D. I. Schuster, A. Blais, L. Frunzio, R.-S. H. J. Majer, S. Kumar, S. M. Girvin, and R. J. Schoelkopf, Nature (London) **431**, 162 (2004).

[14] L. S. Bishop, J. M. Chow, J. Koch, A. A. Houck, M. H. Devoret, E. Thuneberg, S. M. Girvin, and R. J. Schoelkopf, Nature Phys. **5**, 105 (2009).

[15] M. Steffen, M. Ansmann, R. C. Bialczak, N. Katz, E. Lucero, R. McDermott, M. Neeley, E. M. Weig, A. N. Cleland, and J. M. Martinis, Science **313**, 1423 (2006).

[16] J. F. Clauser, M. A. Horne, A. Shimony, and R. A. Holt, Phys. Rev. Lett. **23**, 880 (1969).

[17] J. Koch, T. M. Yu, J. Gambetta, A. A. Houck, D. I. Schuster, J. Majer, A. Blais, M. H. Devoret, S. M. Girvin, and R. J. Schoelkopf, Phys. Rev. A **76**, 042319 (2007).

[18] J. A. Schreier *et al.*, Phys. Rev. B **77**, 180502(R) (2008).

[19] F. Motzoi, J. M. Gambetta, P. Rebentrost, and F. K. Wilhelm, Phys. Rev. Lett. **103**, 110501 (2009).

[20] J. M. Chow, L. DiCarlo, J. M. Gambetta, F. Motzoi, L. Frunzio, S. M. Girvin, and R. J. Schoelkopf, e-print arXiv:1005.1279 [cond-mat].

[21] L. DiCarlo *et al.*, Nature (London) **460**, 240 (2009).

[22] J. Gambetta, A. Blais, D. I. Schuster, A. Wallraff, L. Frunzio, J. Majer, M. H. Devoret, S. M. Girvin, and R. J. Schoelkopf, Phys. Rev. A **74**, 042318 (2006).

[23] D. I. Schuster *et al.*, Nature (London) **445**, 515 (2007).

[24] L. DiCarlo, M. Reed, L. Sun, B. R. Johnson, J. M. Chow, J. M. Gambetta, L. Frunzio, S. M. Girvin, M. H. Devoret, and R. J. Schoelkopf, e-print arXiv:1004.4324 [cond-mat].

[25] R. Horodecki, P. Horodecki, M. Horodecki, and K. Horodecki, Rev. Mod. Phys. **81**, 865 (2009).
[26] D. F. V. James, P. G. Kwiat, W. J. Munro, and A. G. White, Phys. Rev. A **64**, 052312 (2001).
[27] R. Blume-Kohout, New J. Phys. **12**, 043034 (2010).
[28] J. P. Home, D. Hanneke, J. D. Jost, J. M. Amini, D. Leibfried, and D. J. Wineland, Science **325**, 1227 (2009).
[29] J. Eisert, F. G. S. L. Brandao, and K. M. R. Audenaert, New J. Phys. **9**, 46 (2007).
[30] B. S. Cirel'son, Lett. Math. Phys. **4**, 93 (1980).
[31] L. Tornberg, M. Wallquist, G. Johansson, V. S. Shumeiko, and G. Wendin, Phys. Rev. B **77**, 214528 (2008).
[32] C. L. Hutchison, J. M. Gambetta, A. Blais, and F. Wilhelm, Can. J. Phys. **87**, 225 (2009).
[33] L. S. Bishop *et al.*, New J. Phys. **11**, 073040 (2009).
[34] S. Kochen and E. P. Specker, J. Math. Mech. **17**, 59 (1967).
[35] G. Kirchmair, F. Zahringer, R. Gerritsma, M. Kleinmann, O. Guhne, A. Cabello, R. Blatt, and C. F. Roos, Nature (London) **460**, 494 (2009).
[36] H. K. Cummins, G. Llewellyn, and J. A. Jones, Phys. Rev. A **67**, 042308 (2003).
[37] E. Lehmann and G. Casella, *The Theory of Point Estimation*, 2nd ed. (Springer-Verlag, New York, 2003).